IEEE Access
Multidisciplinary | Rapid Review | Open Access Journal

Received 10 May 2023, accepted 16 May 2023, date of publication 26 May 2023, date of current version 6 June 2023.

Digital Object Identifier 10.1109/ACCESS.2023.3280472

RESEARCH ARTICLE

DNN-Based Slip Ratio Estimator for Lugged-Wheel Robot Localization in Rough Deformable Terrains

CHUL-HONG KIM [1,2] AND DONG-IL CHO [1,2,3]

[1]Department of Electrical and Computer Engineering, Seoul National University, Seoul 08826, South Korea
[2]Automation and Systems Research Institute (ASRI), Seoul National University, Seoul 08826, South Korea
[3]Inter-University Semiconductor Research Center (ISRC), Seoul National University, Seoul 08826, South Korea

Corresponding author: Dong-Il Cho (dicho@snu.ac.kr)

This work was supported by the Korea Research Institute for Defense Technology Planning and Advancement (KRIT) funded by the Korean Government through the Defense Acquisition Program Administration (DAPA) (Development of a Platform for Small Scale Ground Robot, in 2022) under Grant KRIT-CT-22-006-01.

ABSTRACT This paper presents a deep neural network (DNN)-based slip ratio estimator fused with an invariant extended Kalman filter (IEKF) for lugged-wheel robot localization using an inertial sensor and an encoder. Among various sensors used in wheeled mobile robot (WMR) localization, inertial sensors and encoders are most commonly used because these sensors are inexpensive and have low computational requirements. However, inertial sensors and encoders can cause large drifts in localization due to inherent sensor characteristics and wheel slippage, respectively. Most studies on wheel slippage have primarily focused on rubber tires, and using this slip ratio model for WMRs with lugged-wheels operating in outdoor environments can result in significant estimation errors in slip ratios. This paper develops a DNN-based slip ratio estimator and IEKF for WMR localization that is robust to wheel slippage even in rugged outdoor environments. The performance of the proposed localization is demonstrated through experiments using outdoor datasets where WMRs with lugged-wheels experience various slip conditions. Experiments are conducted in wet and dry conditions on a sloped grass field. Results show that the proposed localization method reduces accumulated localization errors by 53.5% compared to integration-based localization and by 13.5% compared to IEKF-based localization.

INDEX TERMS Deep learning, encoder, inertial sensor, localization, slip ratio.

I. INTRODUCTION

Encoders, which measure the angular velocity of wheels, are generally used in wheeled mobile robots (WMRs) for robot control and localization [1], [2], [3]. In an ideal condition, encoders can estimate WMR poses with simple kinematic models, but various factors can cause drift errors in reality [4]. Among these factors, wheel slippage is the critical problem that can cause both instantaneous and continuous pose errors in WMR localization. To reduce these errors, other sensors, such as inertial sensors or cameras, should be used with encoders as the data of these sensors are less affected by wheel slippage [5], [6].

A plethora of research has been conducted to estimate wheel slippage. One popular approach is using cameras to observe the surrounding information of the robot to estimate the wheel slippage [5], [7], [8], [9]. The information is used to estimate the velocity of the WMR [5], [7] or classify the terrain characteristics [8], [9], but these methods are limited by heavy computational costs and performance being dependent on luminance and environmental features. Alternatively, inertial sensors have been utilized for wheel slippage estimation [6], [10], [11], [12], [13], but these methods may be affected by sensor accuracy and drift errors. To overcome these limitations, some studies have employed

The associate editor coordinating the review of this manuscript and approving it for publication was Prakasam Periasamy.

machine learning for wheel slippage estimation [10], [11], but estimated wheel slippage was not accurate enough for WMR localization as it only had three defined classes: low slip, moderate slip, and high slip. Another approach is combining localization with robot control by frequently stopping the robot to initialize the accumulated errors [12], [13], but this method limits the degree of freedom in navigation. Since these studies do not concern the characteristic of the wheels of WMR, we propose the WMR localization that comprises the slip ratio estimator designed through the motion analysis of the wheels.

To address wheel slippage in a slippery environment, lugged-wheels are generally used as they can generate more tractive force than rubber tires in rough deformable terrains. Many studies have been conducted to deal with these slippery environments by analyzing the relationship between wheels and terrains [14], [15], [16], [17]. Various factors, such as wheel-terrain interaction models based on normal force, drawbar pull, torque, and shear stress [15], [16], [17], [18], [19], parameter specification of a lug [20], and terrain types [21], have been analyzed. These analyses were evaluated by discrete element method simulations or experiments. However, these studies focus primarily on improving the control performance of WMRs rather than the localization performance. Therefore, we analyzed the motion of the lugged-wheel, which experiences the various phenomena of slippage (slipping, spinning, and skidding), to estimate the slip ratio of the lugged-wheel using inertial sensors and encoders for WMR localization.

This paper presents a deep neural network (DNN)-based slip ratio estimator for the lugged-wheel robot localization using an inertial sensor and an encoder. The DNN-based slip ratio estimator, which comprises a CNN, a FC layer, and a smoothing filter, uses sequential data from an inertial sensor and an encoder to estimate the slip ratio of wheels. To limit the range of estimated slip ratios, the range of slip ratios is divided by the total number of classes, and the split range is assigned to each class. The smoothing filter is used to learn the relationship between consecutive classes. The estimated slip ratio is used as a pseudo measurement of the invariant extended Kalman filter (IEKF)-based localization to estimate the robot pose. The performance of the proposed localization is demonstrated through experiments using outdoor datasets where the robot experiences various slip conditions. The main contribution of this paper is as follows:

- The motion of the lugged-wheel is analyzed using the Euler-Lagrange equation to validate the usage of inertial sensors and encoders for calculating slip ratio.
- Instead of calculating the slip ratio, the DNN-based slip ratio estimator is designed to analyze the pattern of sensors to estimate the slip ratio.
- The DNN-based slip ratio estimator reduces the accumulated error by limiting the range of estimated slip ratios and eliminating the previously estimated results in the input.

The rest of the paper is organized as follows: Section II presents the related work. Section III presents the analysis of the lugged-wheel motion. Section IV presents the structure of the proposed method. Section V discusses the experimental setup and result. Finally, Section VI presents the conclusion.

II. RELATED WORK

For localization, various sensors, such as light detection and ranging (LiDAR) sensors, cameras, inertial sensors, and encoders, are widely used [22], [23], [24], [25], [26]. Among these sensors, inertial sensors and encoders are generally used for WMRs because these sensors are inexpensive compared to other sensors and have low computational requirements. However, inertial sensors and encoders are usually used with additional sensors in robot localization because of their low performance [27], [28], [29], [30], [31]. In the localization technique, accumulated localization errors should be reduced to achieve high performance. For LiDAR sensors and cameras, consecutive frames of sensor data depend on each other as these sensors measure surrounding environments. Therefore, the localization method based on these sensors can reduce the accumulated error by optimizing robot poses using data from the surrounding environment. In contrast, for inertial sensors and encoders, all frames of sensor data are independent, as these sensors measure the instantaneous movement of robots. Therefore, the accumulated localization error based on inertial sensors and encoders highly depends on sensor noises.

Recently, DNN has been used in many research areas, including localization [4], [32], [33], [34], [35], [36], [37], [38], [39], [40], [41]. Some localization research uses only inertial sensors and encoders by using DNN to reduce sensor noise. These studies can be separated into two methods. The first method is fusing DNN and model-based localization such as EKF [37], [38]. The DNN is usually used to solve the problem difficult for model-based localization. The second method is end-to-end DNN-based localization [4], [39], [40]. Only DNN structures are used to estimate robot poses. Various kinds of networks, such as a convolutional neural network (CNN), recurrent neural network (RNN), and long short-term memory (LSTM), can be used for localization. Among these networks, CNNs can be used to estimate the noise of sequential data [38], [41]. In this paper, the proposed method fuses the DNN with IEKF, and DNN is designed to estimate the wheel slippage which is difficult to calculate with the kinematic model. The CNN is used to analyze the slip pattern and reduce the sensor noise of inertial sensors and encoders.

III. ANALYSIS OF LUGGED-WHEEL MOTION

In the localization based on inertial sensors and encoders, robot poses are estimated by the integration. To accurately estimate robot poses, sensors need to either have a high data rate or measure the average data over the sampling time rather than instantaneous data. Likewise, the average slip ratio should be calculated to estimate robot poses accurately. In this section, we demonstrate the analysis of the

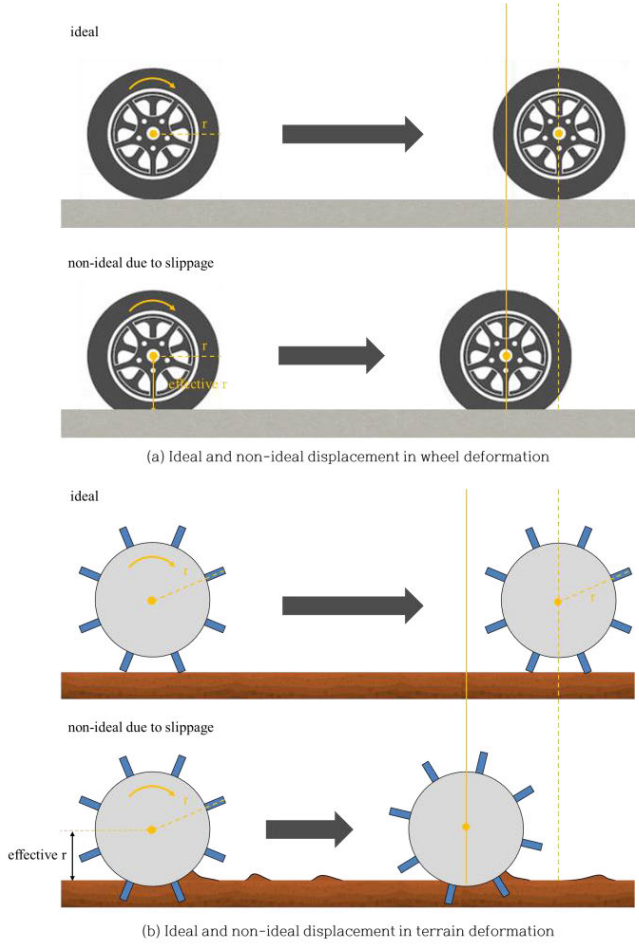

FIGURE 1. Ideal and non-ideal displacement in wheel deformation and terrain deformation. The displacement difference due to slippage is exaggeratedly represented.

lugged-wheel motion to validate the usage of inertial sensors and encoders for calculating the average slip ratio.

The wheel slippage is defined as the difference between the circumferential velocity of the wheel and the actual robot velocity. The slip ratio, which represents the degree of wheel slippage, is calculated to estimate the wheel slippage as the slip ratio and encoder data can be directly used to calculate the robot velocity. The following equation is used to calculate the slip ratio [4], [5], [6], [12], [13], [21]:

$$\lambda = \begin{cases} \dfrac{r\omega - v}{r\omega} & , r\omega \geq v \\ -\dfrac{v - r\omega}{v} & , r\omega < v \end{cases} \tag{1}$$

where λ is the slip ratio, v is the velocity of the robot, r is the radius of the wheel, and ω is the angular velocity of the wheel. The slip ratio is primarily influenced by three factors which are wheel deformation, terrain deformation, and sliding between wheel and terrain. The deformation of the wheel and the terrain, shown in Figure 1, causes the change in the effective radius of the wheel, whereas the sliding between the wheel and the terrain causes the difference between wheel velocity and robot velocity.

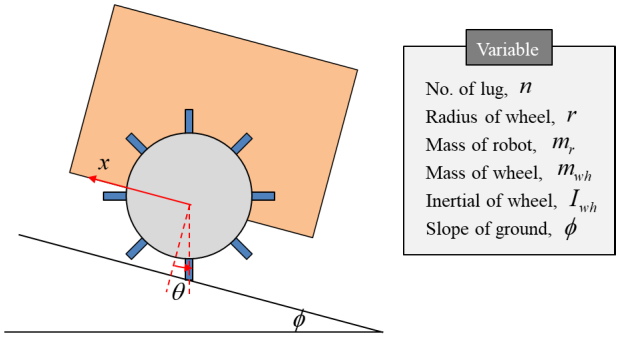

FIGURE 2. The model and variable of the lugged-wheel motion.

Generally, (1) is used to calculate the slip ratio of rubber tires. Among the factors that cause wheel slippage, the slip ratio of rubber tires is primarily caused by the deformation of wheels. Since the deformation of rubber tires does not change instantaneously, (1) is appropriate to estimate the average slip ratio of tires when inertial sensors and encoders are used.

Unlike rubber tires, the slip ratio of a lugged-wheel is primarily caused by the deformation of the terrain and the sliding between the wheel and the terrain. The sliding can be described in two cases (wheel spin and skid). The wheel spin occurs when the wheel spins out from the ground during fast acceleration. The wheel skid occurs when the wheel slides on the ground during fast braking. Since the complex interaction of these factors can cause the instantaneous change in the slip ratio of the lugged-wheel, (1) is inappropriate for estimating the average slip ratio with inertial sensors and encoders. Therefore, the lugged-wheel motion is analyzed using the Euler-Lagrange equation to design the slip model for the lugged-wheel and verify that the slip model can estimate the average slip ratio of robots using an inertial sensor and an encoder.

A. DYNAMIC MODEL OF LUGGED-WHEEL

The Euler-Lagrange equations are a system of second-order ordinary differential equations derived using Lagrange's equation, $L = T*-V$, where T is kinetic energy and V is potential energy [42]. In this section, the Euler-Lagrange equation is used to find the differential equation of the robot and wheel, which are the acceleration of the robot and the angular acceleration of the wheel for the simulation. The coordinates and variables for the analysis of the lugged-wheel motion are shown in Figure 2. As the lugged-wheel motion has three different cases, these are independently analyzed to find the corresponding Euler-Lagrange equation of the robot's and wheel's motion. These cases are detailed as follows. First is a no-slip case when the actual robot velocity is equal to the circumferential velocity of wheels. Second is a wheel slippage case when the actual robot velocity is not equal to the circumferential velocity of wheels. The third

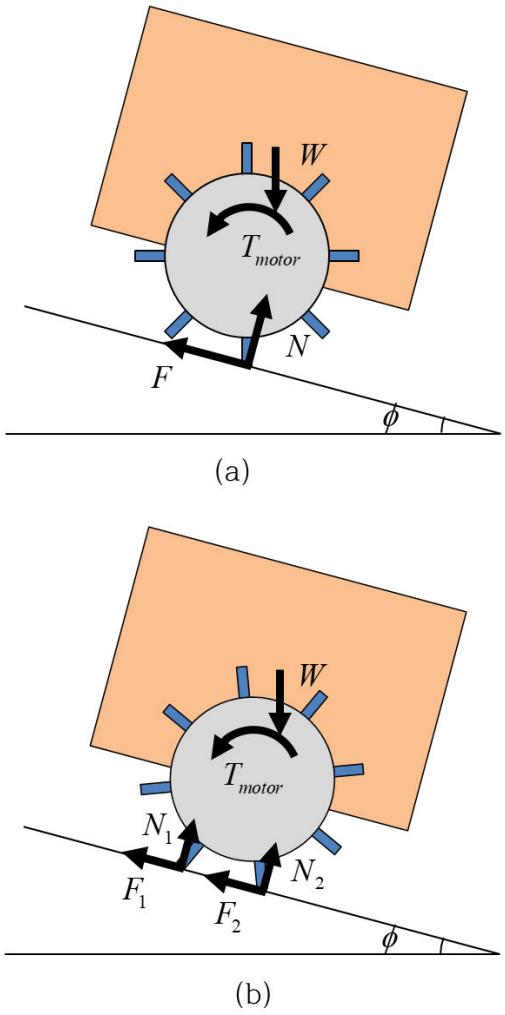

FIGURE 3. The force and torque acting on the lugged-wheel and robot for (a): case 1,2 and (b): case 3.

occurs when two lugs touch the ground at the same time. For the remaining paper, a no-slip case, a slip case, and a two-lugs case represent these three cases, respectively. The robot and the external force acting on the lugged-wheel are shown in Figure 3. Figure 3 (a) shows the external force of two cases, the no-slip case and the slip case, whereas Figure 3 (b) shows the external force of the two-lugs case. The generalized coordinates of the lugged-wheel motion are x and θ. The x is the displacement of the robot in a longitudinal direction. The θ is the angle between the lug and the ground. These coordinates can be expressed as follows:

$$\xi_i = x, \theta, -\frac{\pi}{n} \leq \theta < \frac{\pi}{n} \tag{2}$$

For the no-slip case, the external force acting on the robot can be expressed as follows:

$$\Xi_\theta = T_{motor} - Fr\cos\theta + Nr\sin\theta \tag{3}$$

where T_{motor} is the torque of motors, F is the friction between the lug and the ground, r is the radius of the lugged-wheel, and N is the normal force. The kinetic and potential energies of the system are expressed as follows:

$$T^* = \frac{1}{2}\left(m_r + m_{wh}\right)\left(r\dot{\theta}\right)^2 + \frac{1}{2}I_{wh}\dot{\theta}^2 \tag{4}$$

$$V = \left(m_r + m_{wh}\right) gr\cos\left(\theta - \phi\right) \tag{5}$$

where m_r and m_{wh} are the mass of the robot and the lugged-wheel, I_{wh} is the moment of inertia of the lugged-wheel, g is the gravity, and ϕ is the slope of the ground. As the actual robot velocity is equal to the circumferential velocity of wheels for the no-slip case, the derivative calculation in the Euler-Lagrange equation is derived only for one coordinate, θ. The differential equation of the θ is expressed as follows:

$$\ddot{\theta} = \frac{1}{\left(I_{wh} + \left(m_r + m_{wh}\right) r^2\right)}\left(\left(m_r + m_{wh}\right) gr\sin\left(\theta - \phi\right) + T_{motor} - Fr\cos\theta + Nr\sin\theta\right) \tag{6}$$

For the slip case, the external force acting on the robot can be expressed as (3) and the following additional equation:

$$\Xi_x = F \tag{7}$$

The kinetic and potential energies of the system are expressed as follows:

$$T^* = \frac{1}{2}\left(m_r + m_{wh}\right)\dot{x}^2 + \frac{1}{2}\left(m_r + m_{wh}\right)\left(r\dot{\theta}\sin\theta\right)^2 + \frac{1}{2}I_{wh}\dot{\theta}^2 \tag{8}$$

$$V = \left(m_r + m_{wh}\right) gr\cos\theta\cos\phi + \left(m_r + m_{wh}\right) gx\sin\phi \tag{9}$$

As the actual robot velocity is not equal to the circumferential velocity of wheels for the slip case, the derivative calculation in the Euler-Lagrange equation is derived for coordinates, x and θ. The differential equation of the x and θ can be derived as follows:

$$\ddot{x} = \frac{1}{\left(m_r + m_{wh}\right)}\left(F - \left(m_r + m_{wh}\right) g\sin\phi\right) \tag{10}$$

$$\ddot{\theta} = \frac{1}{\left(I_{wh} + \left(m_r + m_{wh}\right) r^2\sin^2\theta\right)}\Big(-\left(m_r + m_{wh}\right) r^2\dot{\theta}^2\sin\theta\cos\theta + \left(m_r + m_{wh}\right) gr\sin\theta\cos\phi + T_{motor} - Fr\cos\theta + Nr\sin\theta\Big) \tag{11}$$

For the two-lugs case, the external force acting on the robot can be expressed as follows:

$$\Xi_x = F_1 + F_2 \tag{12}$$

$$\Xi_\theta = T_{motor} - F_1 r\cos\theta - F_2 r\cos\left(\theta - \frac{\pi}{2}\right) + N_1 r\sin\theta + N_2 r\sin\left(\theta - \frac{\pi}{2}\right) \tag{13}$$

The kinetic and potential energies of the two-lugs case are equal to (8) and (9), and the differential equation of the x and

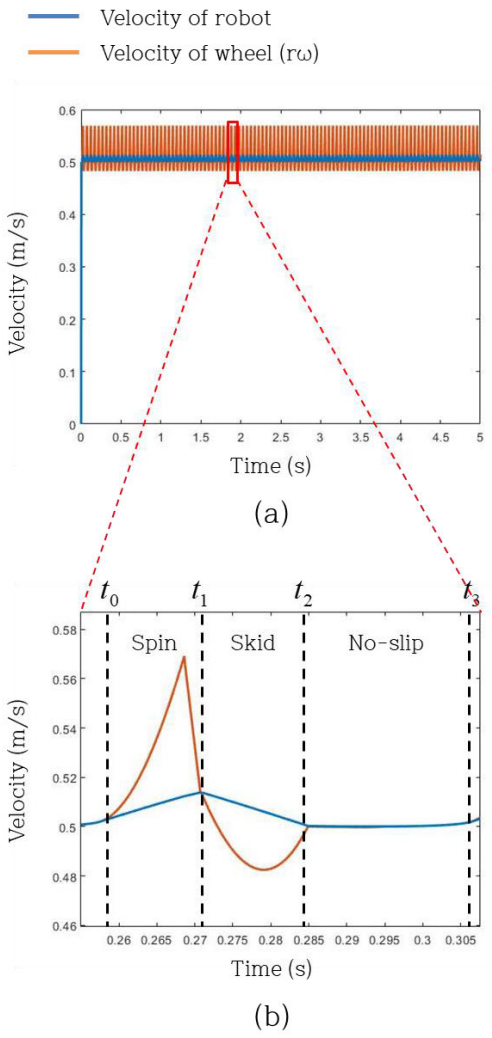

FIGURE 4. Velocity of the robot and the lugged-wheel for simulation.

θ can be derived as follows:

$$\ddot{x} = \frac{1}{(m_r + m_{wh})}\left(F_1 + F_2 - (m_r + m_{wh})\, g \sin\phi\right) \tag{14}$$

$$\begin{aligned}\ddot{\theta} = {} & \frac{1}{\left(I_{wh} + (m_r + m_{wh})\, r^2 \sin^2\theta\right)} \\ & \Big(-(m_r + m_{wh})\, r^2 \dot{\theta}^2 \sin\theta\cos\theta \\ & + (m_r + m_{wh})\, gr \sin\theta\cos\phi + T_{motor} - F_1 r\cos\theta \\ & - F_2 r\cos\left(\theta - \frac{\pi}{n}\right) + N_1 r\sin\theta + N_2 r\sin\left(\theta - \frac{\pi}{n}\right)\Big)\end{aligned} \tag{15}$$

B. SIMULATION OF LUGGED-WHEEL MOTION

In Section III-A, the Euler-Lagrange equation is used to determine the acceleration of the robot and the angular acceleration of the wheel for three different cases. Subsequently, these values are used to calculate the robot's velocity and the wheel's angular velocity of the next frame, with a frame duration of 1 microsecond. By repeatedly calculating these states, the simulation of lugged-wheel motion is conducted to evaluate the suitability of using inertial sensors and encoders for calculating the slip ratio of the lugged-wheel.

For the simulation, several parameters were specified, including the wheel radius, the lug length, the number of lugs, the mass of the robot, the mass of the wheel, and the torque of the wheel. The values for the wheel radius, the lug length, the number of lugs, and the mass of the robot are determined based on the robot platform for the experiment in Section V. The mass of the wheel is set to a value proportional to the mass of the robot with a ratio of 1:6. The constant torque of the wheel is heuristically set to converge the velocity of the robot to 0.5 m/s. The focus of the simulation is to analyze the spin and skid of the wheels, which have a greater slip ratio compared to the slip of wheels. So, the simulation does not consider the deformation of wheels and terrain. To evaluate the slip ratio of the wheel, it is necessary to compare the velocity of the robot with the circumferential velocity of the wheel calculated using the angular velocity of the wheel. The circumferential velocity of wheels is called the velocity of the wheel for the remaining paper. Figure 4 shows the simulation result. Spin occurs when the robot velocity is slower than the velocity of the wheel, whereas skid occurs when the robot velocity is faster than the velocity of the wheel. As shown in Figure 4 (a), spin and skid occur periodically. The frequency of this period is equal to the frequency of each lug touching the ground. As shown in Figure 4 (b), spin, skid, and no-slip conditions occur during a short time. As a result, the slip ratio of the robot changes significantly in an instant.

To improve robot localization, it is necessary to calculate the average slip ratio of the wheels to reduce pose errors when using encoders. To accurately calculate the average slip ratio, the overall slip ratio of the wheels for a single periodic pattern needs to be observed. Figure 4 (b) shows the one periodic pattern of the velocities of the robot and wheel. This pattern can be divided into three parts: a spin part, a skid part, and a no-slip part. The times, $t_0 \sim t_3$, are the boundary of each region. The average velocity of the robot can be expressed as follows:

$$\begin{aligned}\bar{v} &= \frac{D_{spin} + D_{skid} + D_{no-slip}}{t_3 - t_0} \\ &= \frac{\int_{t_0}^{t_1} v(t)\, dt + \int_{t_1}^{t_2} v(t)\, dt + \int_{t_2}^{t_3} v(t)\, dt}{t_3 - t_0}\end{aligned} \tag{16}$$

where D is the displacement of the robot. Let the spin ratio and skid ratio of each part be expressed as follows:

$$\lambda_{spin} = 1 - \frac{\int_{t_0}^{t_1} v(t)\, dt}{\int_{t_0}^{t_1} r\omega(t)\, dt} \tag{17}$$

$$\lambda_{skid} = \frac{\int_{t_1}^{t_2} v(t)\, dt}{\int_{t_1}^{t_2} r\omega(t)\, dt} - 1 \tag{18}$$

where the spin ratio is the slip ratio of the spin part, and the skid ratio is the slip ratio of the skid part. Let the average angular velocity of the lugged-wheel for each part be

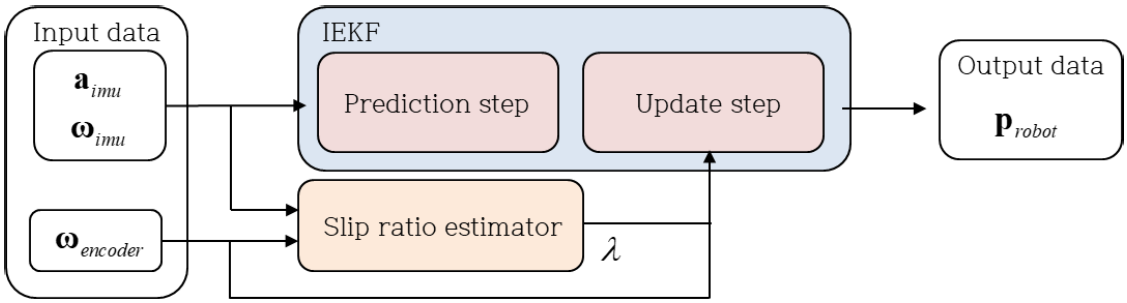

FIGURE 5. Overall structure of proposed localization.

expressed as follows:

$$\bar{\omega}_{spin} = \bar{\omega} + \Delta_{spin}, \bar{\omega}_{skid} = \bar{\omega} - \Delta_{skid}, \bar{\omega}_{no-slip} = \bar{\omega} + \Delta_{no-slip}, \tag{19}$$

the average velocity of the robot can be expressed as in (20), shown at the bottom of the page.

Hence, the average slip ratio can be expressed as follows:

$$\bar{v} \approx \left(1 - \bar{\lambda}\right) r\bar{\omega}, \bar{\lambda} = \left(\frac{(t_1 - t_0)}{t_3 - t_0}\lambda_{spin} - \frac{(t_2 - t_1)}{t_3 - t_0}\lambda_{skid}\right) \tag{21}$$

To calculate the average slip ratio of the robot, the spin ratio and skid ratio should be calculated. Additionally, the duration of the spin, skid, and no-slip parts should be measured according to (21). Each part should be measured at least two times by sensors to approximately estimate the spin and skid according to the Nyquist-Shannon sampling theorem. However, this data rate may be insufficient to measure the duration of each part. Furthermore, the frequency of this cycle and the duration of each region can vary depending on various factors, such as the angular velocity of wheels and characteristics of deformable terrain. Therefore, it is difficult to calculate the average slip ratio of the robot accurately.

IV. PROPOSED LOCALIZATION METHOD

A. OVERALL STRUCTURE

This paper proposes the inertial sensor- and encoder-based robot localization using a DNN-based slip ratio estimator. The overall structure of the robot localization is shown in Figure 5. The robot localization comprises the IEKF and the DNN-based slip ratio estimator. Inertial sensor data are used as input data to the prediction step of the IEKF and the DNN-based slip ratio estimator, and encoder data are used as input data to the update step of the IEKF and the DNN-based slip ratio estimator. The DNN-based slip ratio estimator is used to estimate the slip ratio by analyzing the sensor data pattern instead of calculating the slip ratio. To analyze the sensor data pattern, the n^{th} number of sequential data is used for the input. The IEKF is used to estimate the velocity and orientation of the robot. The update step of the IEKF uses pseudo measurements which are the estimated velocity, the roll, and the pitch of the robot. The estimated velocity is calculated by the slip ratio and encoder data. The roll and pitch of the robot are estimated by the accelerometer. Finally, the velocity and orientation of the robot of the IEKF state are used to calculate the robot pose.

B. STRUCTURE OF IEKF

The proposed method estimates the robot localization based on IEKF using inertial sensors and encoders. The state and prediction step of the IEKF are inspired by the localization method of IEKF [6], [43], [44], and the pseudo-measurement of the IEKF is inspired by the paper of Brossard [38]. Figure 6 shows the coordinate system, which contains world and robot frames. We define a world frame, W(OXYZ), and a robot frame, R(oxyz). Lie group geometry transforms the rotation matrix from a three-axis orientation.

The inertial sensor comprises an accelerometer and gyroscope, which measure the three-axis acceleration and three-axis angular velocity of robots. The orientation of robots in the world frame can be calculated using angular velocities, and the velocity of robots in the world frame can be

$$\begin{aligned}\bar{v} &= \left(1 - \frac{(t_1 - t_0)}{t_3 - t_0}\lambda_{spin} + \frac{(t_2 - t_1)}{t_3 - t_0}\lambda_{skid}\right) r\bar{\omega} \\ &\quad + \left(\frac{\left(1 - \lambda_{spin}\right) r\Delta_{spin}\,(t_1 - t_0) - \left(1 + \lambda_{skid}\right) r\Delta_{skid}\,(t_2 - t_1) + r\Delta_{no-slip}\,(t_3 - t_2)}{t_3 - t_0}\right) \\ &\approx \left(1 - \frac{(t_1 - t_0)}{t_3 - t_0}\lambda_{spin} + \frac{(t_2 - t_1)}{t_3 - t_0}\lambda_{skid}\right) r\bar{\omega}, \\ &\bar{\omega} \gg \Delta_{spin}, \Delta_{skid}, \ \Delta_{no-slip}\end{aligned} \tag{20}$$

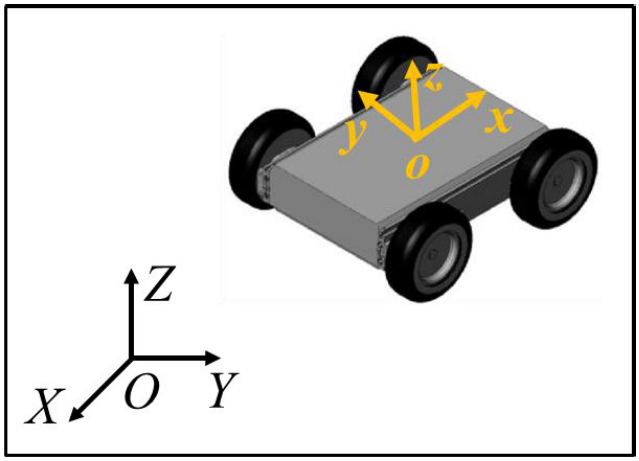

FIGURE 6. Coordinate system where OXYZ represents the world frame and oxyz represents the lugged-wheel robot frame.

calculated using accelerations and orientation of robots with the following kinematic motion equations:

$$\mathbf{v}_{W,k} = \mathbf{v}_{W,k-1} + \Delta t \left(\mathbf{R}^W_{R,k-1} \mathbf{a}_{R,k} + \mathbf{g} \right) + \mathbf{w}_k \tag{22}$$

$$\mathbf{R}^W_{R,k} = \mathbf{R}^W_{R,k} \cdot e^{\Delta t \omega_{R,k} + \mathbf{w}_k} \tag{23}$$

where $\mathbf{v}$ is the velocity of the robot, $\mathbf{R}$ is the rotation matrix of the robot. The $\mathbf{a}$ and ω are three-axis acceleration and three-axis angular velocity measured by the inertial sensor, respectively. The Δt is the time interval between measurements. The $\mathbf{w}$ represents zero-mean Gaussian noises. The rotation matrix of the robot in the Lie group can be expressed as the three-axis orientation of the robot in Lie algebra with the following equations:

$$\mathbf{R}^W_R = e^{\theta_W}, \theta_W = \begin{bmatrix} \phi_W & \theta_W & \psi_W \end{bmatrix}^T \tag{24}$$

where ϕ, θ, and ψ are the roll, pitch, and yaw of robots. The three-axis acceleration, $\mathbf{a}$, and three-axis angular velocity, ω, are inertial sensor data, which can be represented as follows:

$$\mathbf{u}_k = \begin{bmatrix} \mathbf{a}^T_k & \omega^T_k \end{bmatrix}^T = \begin{bmatrix} a_x & a_y & a_z & \omega_x & \omega_y & \omega_z \end{bmatrix}^T \tag{25}$$

The pseudo-measurements are used in the update step of IEKF instead of observation measurements. The pseudo-measurements comprise five inputs which are the three-axis velocity of robot in the robot frame and the roll, pitch of the robot in the world frame. The directions of three-axis velocity are longitudinal, lateral, and vertical in the robot frame. The longitudinal velocity is estimated by the slip ratio and encoder data, while the lateral and vertical velocities are set to zero. The roll and pitch of the robot are calculated using the accelerometer by estimating the direction of gravity. The measurement model is expressed as follows:

$$h\left(\mathbf{x}_{k|k-1}\right) = \begin{bmatrix} \left(\mathbf{R}^W_{R,k|k-1}\right)^T \mathbf{v}_{W,k|k-1} \\ \phi_{W,k} \\ \theta_{W,k} \end{bmatrix} \tag{26}$$

We define the state of IEKF as follows:

$$\mathbf{x} = \begin{Bmatrix} \mathbf{v}_W & \mathbf{R}^W_R \end{Bmatrix} \tag{27}$$

To estimate the velocity and orientation of the robot, the prediction step ($\hat{x}_{k|k-1}$) and update step ($\hat{x}_{k|k}$) of IEKF for the system, (22), (23), and (26), are recursively used as follows:

$$\hat{\mathbf{x}}_{k|k-1} = \hat{\mathbf{x}}_{k-1|k-1} + \Delta t \cdot f\left(\hat{\mathbf{x}}_{k-1|k-1}, \mathbf{u}_k\right) \tag{28}$$

$$\mathbf{P}_{k|k-1} = \mathbf{F}_k \left(\mathbf{P}_{k-1|k-1} + \mathbf{G}_k \mathbf{Q}_k \mathbf{G}^T_k \right) \mathbf{F}^T_k \tag{29}$$

$$\mathbf{K}_k = \mathbf{P}_{k|k-1} \mathbf{H}^T_k \left(\mathbf{H}_k \mathbf{P}_{k|k-1} \mathbf{H}^T_k + \mathbf{V} \right)^{-1} \tag{30}$$

$$\hat{\mathbf{x}}_{k|k} = \hat{\mathbf{x}}_{k|k-1} + \mathbf{K}_k \left[\mathbf{y}_k - \mathbf{h}\left(\hat{\mathbf{x}}_{k|k-1}\right) \right] \tag{31}$$

$$\mathbf{P}_{k|k} = \left(\mathbf{I}_6 - \mathbf{K}_k \mathbf{H}_k\right) \mathbf{P}_{k|k-1} \tag{32}$$

where $\mathbf{F}$ and $\mathbf{G}$ are the Jacobians of the motion model, f, with respect to states, $\mathbf{x}$, and inputs, $\mathbf{u}$. $\mathbf{V}$ is the covariance of pseudo-measurement units. $\mathbf{Q}$ is the covariance of the inertial sensor:

$$\mathbf{e}_k = \mathbf{y}_k - h\left(\mathbf{X}_{k|k-1}\right) \tag{33}$$

$$\mathbf{Q}_0 = \begin{bmatrix} \sigma^2_1 \mathbf{I}_3 & \cdots \\ \cdots & \sigma^2_2 \mathbf{I}_3 \end{bmatrix} \tag{34}$$

$$\mathbf{Q}_k = \gamma \mathbf{e}^T_k \mathbf{e}_k \mathbf{Q}_0 + \mathbf{Q}_0 \tag{35}$$

where $\mathbf{e}$ is the error of measurement, σ is the covariance of the accelerometer and gyroscope, and γ is the heuristic parameter for the measurement unit. The calculation of $\mathbf{Q}$ is inspired by the paper [6]. The covariance of pseudo-measurement is set heuristically using the experimental result of outdoor datasets mentioned in Section V. After the update step, the additional calculation is executed to estimate the position of the robot.

$$\mathbf{p}_{W,k} = \mathbf{p}_{W,k-1} + \Delta t \hat{\mathbf{v}}_{W,k|k} \tag{36}$$

where $\mathbf{p}$ is the position of the robot in the world frame.

In the IEKF, pseudo-measurements are used to reduce errors in the states. For inertial sensor- and encoder-based localization, the most important pseudo-measurement is the longitudinal velocity of the robot, which can have significant localization errors due to wheel slippage. Therefore, it is important to estimate the slip ratio accurately. As inertial sensors are not affected by wheel slippage, while encoders are, the slip ratio can be calculated using the following equation:

$$\lambda = 1 - \frac{v_{R,k|k-1,lon}}{\omega_{encoder} r} \tag{37}$$

where v is the longitudinal velocity of the robot after the prediction step in the robot frame, $\omega_{encoder}$ is the encoder data, and r is the wheel radius. However, accurately calculating the slip ratio can be challenging, as mentioned in section III. Additionally, the slip ratio calculation involves the previously estimated velocity, which can result in accumulated errors. To address this, we propose a DNN-based slip ratio estimator. The proposed estimator analyzes sensor data patterns to estimate the slip ratio, and its inputs do not include the previously estimated velocity to prevent the accumulation of errors.

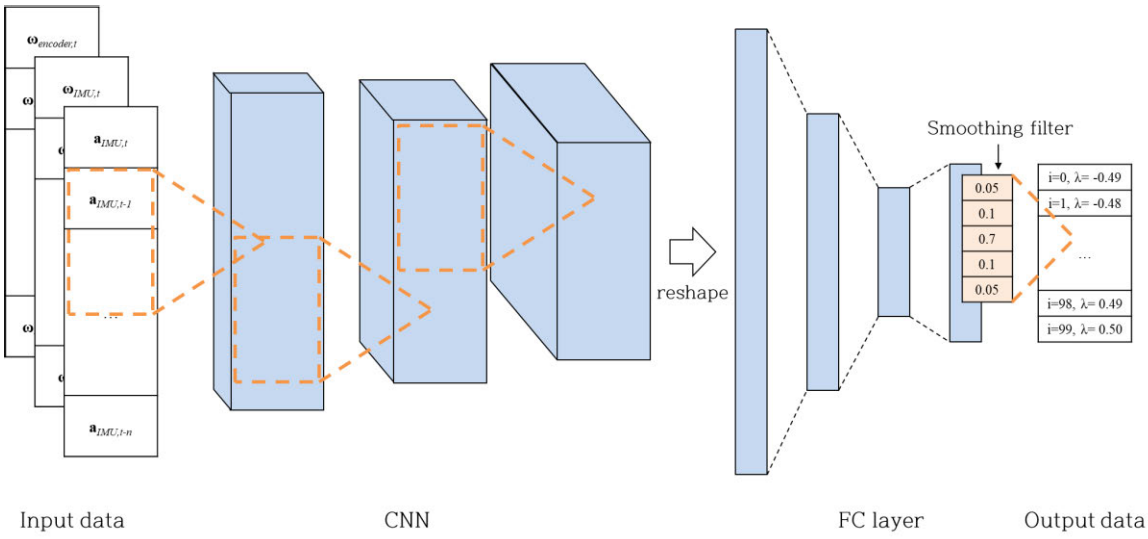

FIGURE 7. Overall structure of DNN-based slip ratio estimator.

C. DNN-BASED SLIP RATIO ESTIMATOR

We proposed the DNN-based slip ratio estimator for accurate slip ratio estimation. Two points are considered to design the structure of the DNN-based slip ratio estimator. Firstly, the DNN-based slip ratio estimator is designed to learn patterns of sensor data, which depends on the average slip ratio because it is difficult to calculate the average slip ratio of robots accurately, as mentioned in Section III. Secondly, the DNN-based slip ratio estimator is designed to eliminate the effect of previous states to reduce the accumulated error because the proposed network does not rely on learning a kinematic model for calculating the slip ratio. Therefore, to estimate the average slip ratio of robots by analysis, a DNN-based slip ratio estimator uses sequential data of three-axis acceleration and three-axis angular velocity of the inertial sensor, and two-axis angular velocity of the encoder. The input data length is set to balance between two factors. First, the data length should be long enough to allow the DNN to analyze the pattern and predict the accurate slip ratio. Second, the data length should be short enough to avoid including the acceleration and deceleration of the robot within a single sequence of data. This is important to prevent the network from learning the robot's trajectory rather than the slip ratio. The DNN-based slip ratio estimator comprises three parts to estimate the average slip ratio, which are 1D CNNs, fully connected (FC) layers, and a smoothing filter, as shown in Figure 7.

The input data of the DNN-based slip ratio estimator are the sequential data of the inertial sensor and encoder. As the purpose of the DNN-based slip ratio estimator is to estimate the average slip ratio of the robot rather than the instantaneous slip ratio, the sequential data are used to analyze the sensor data pattern. The 1D CNN is used to analyze the data pattern of the inertial sensor and encoder as it is specialized to extract the feature of sequential data. Table 1 presents the detail of the 1D CNN.

TABLE 1. Detail of the CNN.

Layer	Input	CNN#1	CNN#2	CNN#3
Data length	32	26	20	14
Kernel size	-	7	7	7
Channel dim.	8	16	32	64

TABLE 2. Detail of the FC layer.

Layer	CNN#3	FC#1	FC#2	FC#3
Node size	896	512	64	100

$$x_{cnn} = \text{CNN}\left(\mathbf{a}_{IMU,t-N}, \cdots, \mathbf{a}_{IMU,t}, \omega_{IMU,t-N}, \cdots, \omega_{IMU,t}, \omega_{encoder,t-N}, \cdots, \omega_{encoder,t}\right) \tag{38}$$

The FC layer is used to estimate the average slip ratio of the robot by classification. RNN and LSTM are commonly used for pose-related results [39], [40], but the DNN-based slip ratio estimator does not use these networks for two reasons. Firstly, these networks are used to learn kinematics. Secondly, these networks use previous states to estimate the next state. As the purpose of the proposed network is not to learn kinematics and not to use previous states, the proposed network only uses FC layers to estimate the slip ratio. For the output of the FC layer, the classification is used as it can limit the range of the estimated slip ratio to reduce the accumulated error and match the analyzed sensor patterns to the belonging slip ratio. The detail of the FC layer is shown in Table 2.

$$y = \text{softmax}\left(\text{CNN}\left(\text{FC}\left(x_{cnn}\right)\right)\right) \tag{39}$$

Using classification does not ensure that errors are estimated near the target slip ratio, as each class is learned

FIGURE 8. Lugged-wheel robots and lugged-wheel.

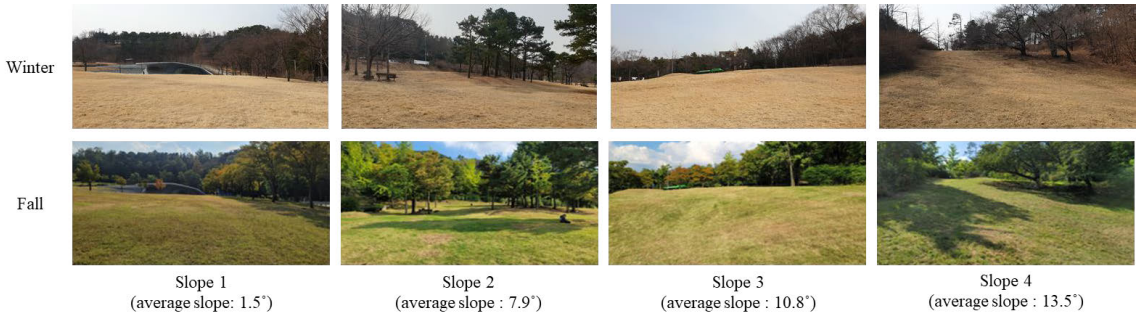

FIGURE 9. Outdoor environments for training datasets.

independently. To prevent this problem, a smoothing filter and smoothing labeling are used to learn the relationship between consecutive classes. For the smoothing filter, a fixed seven kernel size 1D CNN is used. For smoothing labeling, the target data of the class are scored 0.7 and 0.15 to the corresponding and surrounding classes, respectively. The followings are the equation to calculate the corresponding index of the slip ratio and the slip ratio of the index:

$$i = \lfloor (\lambda - 0.005 + 0.5) \times 100 \rfloor \tag{40}$$

$$\lambda = (i - 49) \times 0.01 \tag{41}$$

The slip ratio, which represents the degree of wheel slippage as mentioned earlier, is set from -0.5 to 0.5. The total number of classes is 100, and the resolution of the slip ratio is 0.01.

The entire network is implemented using PyTorch. We trained our network using the AdamW optimizer, setting the initial learning rate to 10^{-4} and weight decay to $10^{-5}10^{-5}$. The training was conducted for 200 epochs with a batch size of 128. NVIDIA GeForce RTX 2080 Ti was used for training. The dropout rate was set to 0.2 for the transformer module.

V. EXPERIMENTS

In this section, there are two types of experiments are conducted. First is an indoor experiment to validate the simulation of lugged-wheel motion using a motion capture system. Second is an outdoor experiment to evaluate the proposed method. As the proposed method includes the DNN to estimate the slip ratio, the training methodology, validation, and experimental results of outdoor experiments are explained in each subsection.

FIGURE 10. Outdoor environments for testing datasets.

Section V is organized as follows: Subsection A presents the overall experimental setup for both indoor and outdoor experiments. Subsection B presents the validation result of the simulation based on indoor experiments. Subsection C presents the training methodology. Subsection D presents the validation result of outdoor experiments. Subsection E presents the experimental results. Subsection F presents the computing time of the proposed method compared to others. Finally, subsection G presents the future work of the proposed method.

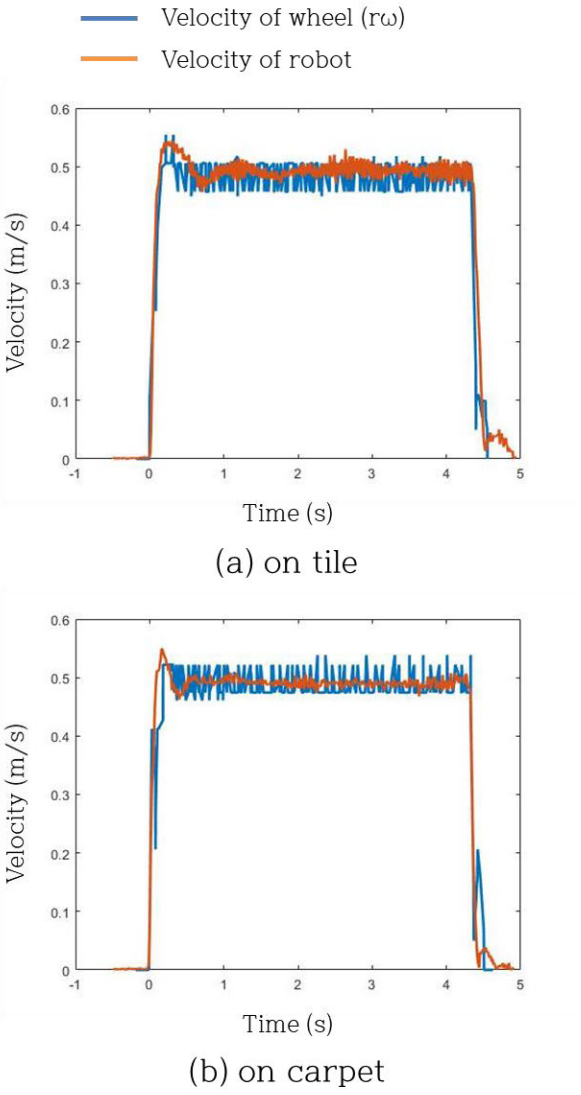

FIGURE 11. Experimental result for velocity of the wheel and robot.

A. EXPERIMENTAL SETUP

We formulate various datasets to evaluate simulation results and the proposed method. All experiments are performed on the desktop computer using self-generated datasets. For the outdoor lugged-wheel robot, two commercial lawnmowers (L7, LG Electronics) are used, shown in Figure 8. In the rest of this paper, the terms ''robot no. 1'' and ''robot no. 2'' are used to refer to two distinct lawnmowers, respectively. The sensors used for the experiment are the MPU-6050 (commercial inertial sensor), which specifications are presented in [45], and the built-in encoder, which has a resolution of 0.025 ms^{-1}. The data rate of the inertial sensor and encoder is 80Hz and 50Hz, respectively.

To evaluate simulation results, the indoor datasets are generated using a motion capture system (Vicon). Two types of floors, a tile and a carpet, are used for indoor datasets. Each condition is repeated four times, so eight datasets are generated to evaluate simulation results. The motion capture system is used to generate the ground truth velocity of the robot. Infrared reflective markers are placed on the robot, and these markers are tracked by the motion capture system with a high accuracy of less than 0.5 mm error.

To train the DNN-based slip ratio estimator, we formulate three dataset types in a sloped outdoor grass environment. Each type has different conditions, so the robot experiences different slip conditions. The first dataset type is generated using robot no. 1 when the grass is dry in the winter. The second dataset type is generated using robot no. 1 when the grass is wet after rain in the winter. The third dataset type is generated using robot no. 2 when the grass is dry in the fall. The outdoor environment for the winter and fall is shown in Figure 9. For each dataset type, four places are chosen with different slopes so that the robot experiences different slip conditions. The robot moves 10 m $\times$ 10 m square trajectory. Each condition is repeated four times, so forty-eight datasets are generated for training.

To evaluate the performance of the DNN-based slip ratio estimator, we formulate three dataset types. Two more places are chosen to avoid the place for the training datasets. The testing datasets have three trajectories which are 10 m $\times$ 10 m square, 10 m $\times$ 10 m zigzag pattern, and 40 m straight line. Each condition is repeated four times, so twelve datasets are generated to evaluate the performance. The outdoor environment for each place of testing datasets is shown in Figure 10.

The proposed method is compared with two other localization methods using an inertial sensor and an encoder. The first method is integration-based localization. The other method is IEKF-based localization using a calculated slip ratio. The structure of IEKF is explained in Section IV-B, which is inspired by [6], [38], [43], and [44], and the slip ratio is calculated by (37). The performance of the localization methods is compared using a closed-loop error which is the distance between the beginning and end poses of the trajectory. For the closed-loop error, we control the robot to place it back to the beginning pose at the end of the datasets.

B. VALIDATION OF SIMULATION

In Section III, we use the analysis and simulation of the lugged-wheel motion to evaluate the validity of calculating the short-term average slip ratio. We conclude that it is hard to calculate the short-term average slip ratio because the high data rate of sensors is required to calculate the spin ratio and skid ratio for accurate estimation. This experiment is conducted to support simulation results. The data rate of the Vicon and encoder sensor is 100Hz and 50Hz, respectively. Figure 11 shows the graph of experimental results. The blue line represents the circumferential velocity of the encoder, whereas the orange line represents the robot velocity measured by the motion capture system. Figure 11 (a) is the experimental result on a tile, while Figure 11 (b) is the experimental result on a carpet. The graph shows that the velocity of both the wheel and robot is measured irregularly for whole datasets. This means that the data rate of 100Hz

is insufficient to calculate the short-term average slip ratio accurately.

C. TRAINING METHODOLOGY

For training, we formulate forty-eight datasets in the three outdoor environments, explained before. These datasets can be classified into three types depending on the ground conditions. Table 3 provides the detail of the training datasets. Dataset no. 1 is a group that uses the robot no. 1 on dry grass in the winter. Dataset no. 2 is a group that uses the robot no. 1 on wet grass in the winter. To satisfy the wet condition, dataset no. 2 is generated one day after 13.4 mm of rain. Dataset no. 3 is a group that uses the robot no. 2 on dry grass in the fall. Each group has different conditions so that the DNN-based slip ratio estimator can learn various slip ratios on various conditions.

To train the proposed network, we plan a specific scheme to evaluate the presence of overfitting. Usually, some of the training datasets are randomly chosen for validation. However, we plan six scenarios to train the DNN-based slip ratio estimator as each group of datasets contains sufficient data to train the proposed network. Each group comprises sixteen datasets, and each dataset contains about ten thousand sequence data composed of three-axis acceleration, three-axis angular velocity, and two-axis wheel speeds. Table 4 provides the detail of the scenario. For each scenario, a different combination of training and validation datasets is used, so training datasets do not include all conditions. This is done to test the generalizability of the proposed DNN-based slip ratio estimator to see if it can accurately estimate the slip ratio in untrained conditions with similar sensors and robots.

For target data of training datasets, the slip ratio of the IEKF-based localization is calculated and customized. The slip ratio of the IEKF-based localization is the instantaneous data calculated by the inertial sensor and encoder. As the purpose of using DNN is to estimate the short-term average slip ratio of the robot rather than the instantaneous slip ratio, a low pass filter is applied to the slip ratio of the IEKF-based localization to eliminate the rapid change in the calculated slip ratio. The lag of the low pass filter is corrected by heuristically compensating the time, which is shifting the time manually. Figure 12 shows an example of the customized slip ratio compared to the calculated slip ratio of the IEKF-based localization.

D. VALIDATION RESULTS

The closed-loop error is calculated to validate the training results of the DNN-based slip ratio estimator. For each scenario, the training and validation datasets have different conditions. We doubt the DNN-based slip ratio estimator being mistrained in two cases. The first case is that the DNN- based slip ratio estimator only works for the robot used in training. Two different robots are used to generate the datasets to check the first case. The second case is that the estimated slip ratio depends on the slope of the ground because the DNN-based slip ratio estimator can learn the slope of the ground, not the slip ratio, from the sensor data. To check the second case, three different ground conditions, dry winter grass, wet winter grass, and dry fall grass, are chosen to generate different slip ratios on the same slope of ground for datasets. Figure 13 shows an example of the validation result for dataset no. 2-13. In Figure 13 (a), the slip ratio of three types is shown: the slip ratio calculated by the IEKF-based localization, the slip ratio estimated by the DNN-based slip ratio estimator, and the customized slip ratio. The slip ratio estimated by the DNN-based slip ratio estimator is closer to the customized slip ratio than that calculated by the IEKF-based localization, indicating that the proposed DNN-based slip ratio estimator is able to effectively analyze the sensor data pattern to estimate the short-term average slip ratio. Figure 13 (b) shows the trajectory of the integration-based localization, the IEKF-based localization, and the proposed method for dataset no. 2-13. Table 5 provides validation results of all training scenarios. As shown in Table 5, the overall validation results of the proposed method are better than that of the integration-based localization. These are similar to or better than that of the IEKF-based localization. Validation results prove that the trained DNN-based slip ratio is not belonging to any cases.

Among validation results, the closed-loop error of scenario no. 6 for slope no. 4 is larger than that of the IEKF-based localization. Scenario no. 6 uses dataset no. 3 for training and dataset no. 1 and 2 for validation. Even though a different robot is used to generate dataset no. 3, validation results of slope no. 1-3 is similar to or better than that of the IEKF-based localization, which is similar to other scenarios. Using a different robot is not the reason for the larger error. As validation results for the datasets of slope no. 4 have larger errors, the slope of the ground is the main cause of the closed-loop

TABLE 3. The detail of training datasets.

Dataset no.		Robot platform	Condition of grass	Slope
1	1-1 ~ 1-4	Robot no. 1	Dry grass in winter	Slope no. 1
	1-5 ~ 1-8			Slope no. 2
	1-9 ~ 1-12			Slope no. 3
	1-13 ~ 1-16			Slope no. 4
2	2-1 ~ 2-4		Wet grass in winter	Slope no. 1
	2-5 ~ 2-8			Slope no. 2
	2-9 ~ 2-12			Slope no. 3
	2-13 ~ 2-16			Slope no. 4
3	3-1 ~ 3-4	Robot no. 2	Dray grass in fall	Slope no. 1
	3-5 ~ 3-8			Slope no. 2
	3-9 ~ 3-12			Slope no. 3
	3-13 ~ 3-16			Slope no. 4

TABLE 4. The detail of the scenario.

	Training datasets	Validation datasets
Scenario no. 1 (s1)	Dataset no. 1, 2	Dataset no. 3
Scenario no. 2 (s2)	Dataset no. 1, 3	Dataset no. 2
Scenario no. 3 (s3)	Dataset no. 2, 3	Dataset no. 1
Scenario no. 4 (s4)	Dataset no. 1	Dataset no. 2, 3
Scenario no. 5 (s5)	Dataset no. 2	Dataset no. 1, 3
Scenario no. 6 (s6)	Dataset no. 3	Dataset no. 1, 2

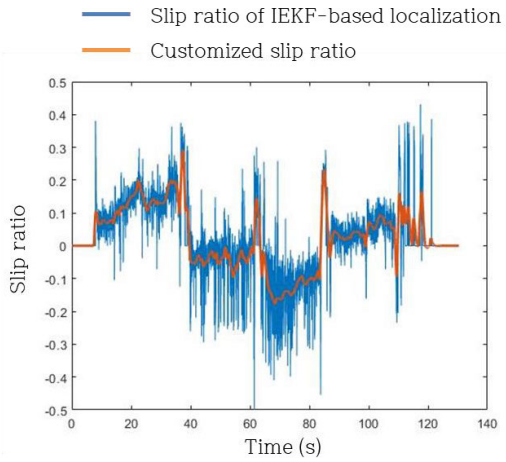

FIGURE 12. Example of slip ratio of IEKF-based localization and customized slip ratio.

error. Slope no. 4 has the biggest inclined angle of the ground, leading to the largest slip ratio. Among the various grass conditions, the short-term average slip ratio of the robot is increasing according to the following order: dry fall grass, dry winter grass, and wet winter grass. Figure 14 shows the slip ratio of the IEKF-based localization for dataset no. 2-13 and 3-13 to show the slip ratio of the robot on wet winter grass and dry fall grass. For scenario no. 6, the slip ratio of dataset no. 3 for slope no. 4 is used for training, which has a lower slip ratio than other datasets. To accurately estimate the slip ratio of dataset no. 1, 2 for slope no. 4, the trained DNN-based slip ratio estimator should estimate the slip ratio beyond the trained range of slip ratio. As a result, closed-loop errors of dataset no. 1, 2 for slope no. 4 are bigger than that of the IEKF-based localization. This shows that the proposed network can only accurately estimate the trained range of slip ratio.

E. EXPERIMENTAL RESULTS

The closed-loop error is calculated to evaluate the performance of the proposed method for testing datasets. The testing dataset is generated using robot no. 2 on dry fall grass in a different place from the training datasets. Some datasets have different trajectories from the training datasets. Table 6 provides the experimental results of the testing datasets. Figure 15 shows the robot trajectories of the integration-based localization, the IEKF-based localization, and the proposed method for dataset no. 4-1, 4-3, 4-5, 4-7, 4-9, and 4-12. The closed-loop error of the proposed method of scenario no. 3 is lower than that of other methods because scenario no. 3 uses both robots and experiences as many different slip conditions as possible. The closed-loop error of the proposed method reduces the accumulated error of the integration-based localization by 53.5% and the IEKF-based localization by 13.5%. Specifically, the closed-loop error of the proposed method for square and zigzag pattern trajectories is similar to or lower

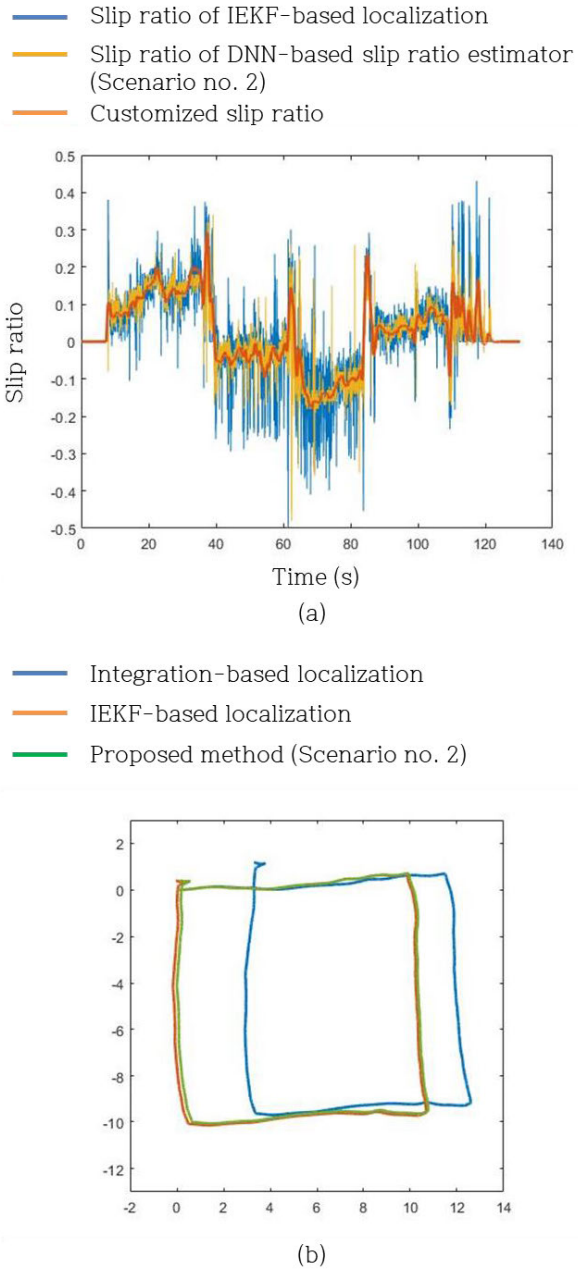

FIGURE 13. Example of validation result. (a) Slip ratio of IEKF-based localization, DNN-based slip ratio estimator, and customized slip ratio for dataset no. 2-13. (b) Trajectories of integration-based localization, IEKF-based localization, and proposed method for dataset no. 2-13.

than that of the IEKF-based localization. In contrast, the closed-loop error of the proposed method for a straight-line trajectory is lower than that of the IEKF-based localization.

The DNN-based slip ratio estimator prevents accumulated errors because of its structure. Experimental results of the DNN-based slip ratio estimator do not have the accumulated error as the input to networks does not contain the previously estimated state. In contrast, as the IEKF-based localization calculated the slip ratio based on the previous

TABLE 5. Validation results.

Dataset no.		Robot platform	Condition of grass	Slope	Closed-loop error (m)							
					Integration-based localization	IEKF-based localization	Proposed method					
							S1	S2	S3	S4	S5	S6
1	1-1~1-4	Robot no. 1	Dry grass in winter	Slope no. 1	1.82	1.02	-	-	1.01	-	1.00	1.01
	1-5~1-8			Slope no. 2	2.60	0.76	-	-	0.66	-	0.64	0.62
	1-9~1-12			Slope no. 3	3.46	0.72	-	-	0.72	-	0.73	0.89
	1-13~1-16			Slope no. 4	3.97	0.67	-	-	0.59	-	0.56	0.95
2	2-1~2-4		Wet grass in winter	Slope no. 1	1.87	0.76	-	0.75	-	0.75	-	0.75
	2-5~2-8			Slope no. 2	2.65	0.66	-	0.55	-	0.54	-	0.60
	2-9~2-12			Slope no. 3	3.13	1.09	-	1.06	-	1.02	-	0.97
	2-13~2-16			Slope no. 4	4.38	0.79	-	0.89	-	0.78	-	1.41
3	3-1~3-4	Robot no. 2	Dry grass in fall	Slope no. 1	1.70	0.77	0.74	-	-	0.76	0.71	-
	3-5~3-8			Slope no. 2	1.63	0.71	0.80	-	-	0.82	0.81	-
	3-9~3-12			Slope no. 3	2.60	0.68	0.72	-	-	0.69	0.73	-
	3-13~3-16			Slope no. 4	4.45	1.34	1.41	-	-	1.38	1.51	-

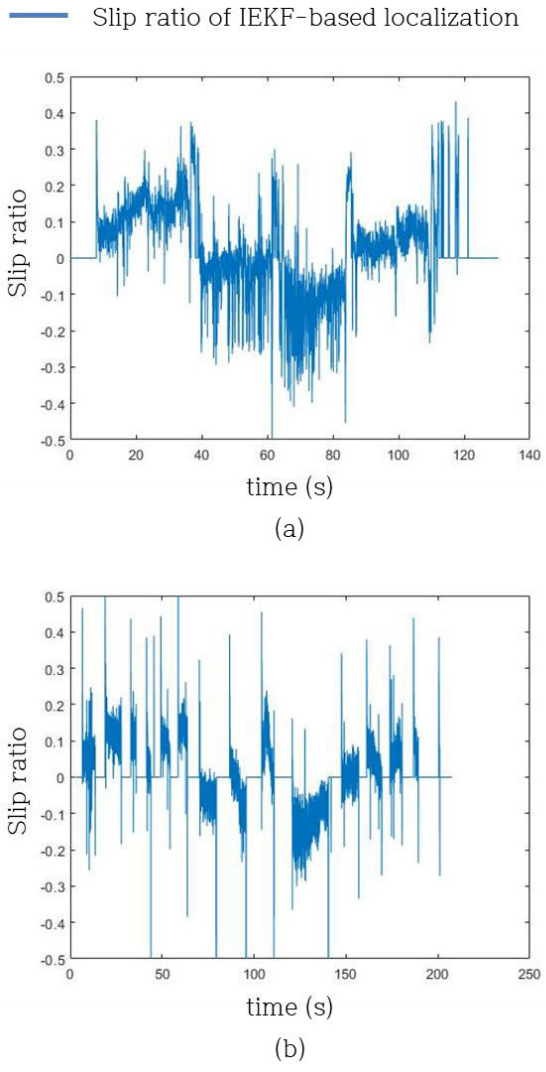

FIGURE 14. Slip ratio of IEKF-based localization for dataset no. 2-13 and 3-13.

velocity of the robot, the calculated slip ratio has the accumulated error. However, the accumulated error is initialized when the robot is stopped. As the accumulated error does not significantly affect the performance of datasets containing 10 m length movement, we formulate the datasets with long-distance movement, 40 m straight-line trajectory, to analyze the accumulated error of the proposed method. To emphasize the effect of the accumulated error, the robot is not stopped when going away, and the robot is frequently stopped when returning, as shown in Figure 16. The slip ratio calculated by the IEKF-based localization and estimated by the DNN-based slip ratio estimator appear similar in Figure 16, but Table 6 shows that the closed-loop error of the proposed method for a straight-line trajectory reduces the accumulated error of the IEKF-based localization by 13.4%, In contrast, the closed-loop error of the proposed method for square and zigzag pattern trajectories only reduces the accumulated error of the IEKF-based localization by 3.8%. These results show that the DNN-based slip ratio estimator effectively prevents the accumulated error.

F. COMPUTING TIME

The disadvantage of using DNN is an increase in the runtime of the algorithm. To evaluate the computing time, the runtime of the integration-based localization, the IEKF-based localization, and the proposed method is measured using Intel Xeon for CPU and NVIDIA GeForce RTX 2080 Ti for GPU. Table 7 provides the runtime of each localization method in microseconds for processing each input of the dataset. The runtime of the proposed method is measured twice, once using the CPU and once using the GPU. The runtime of the proposed method using the CPU is 1.2 kHz, which is greater than the data rate of sensors, but the computing time of the proposed method increases about 20.7 times compared to IEKF-based localization.

G. FUTURE WORK

In future work, there are two approaches to be further investigated. The first is investigating the effect of using multiple inertial sensors for further improvement. The second is investigating the potential of using simulated datasets to

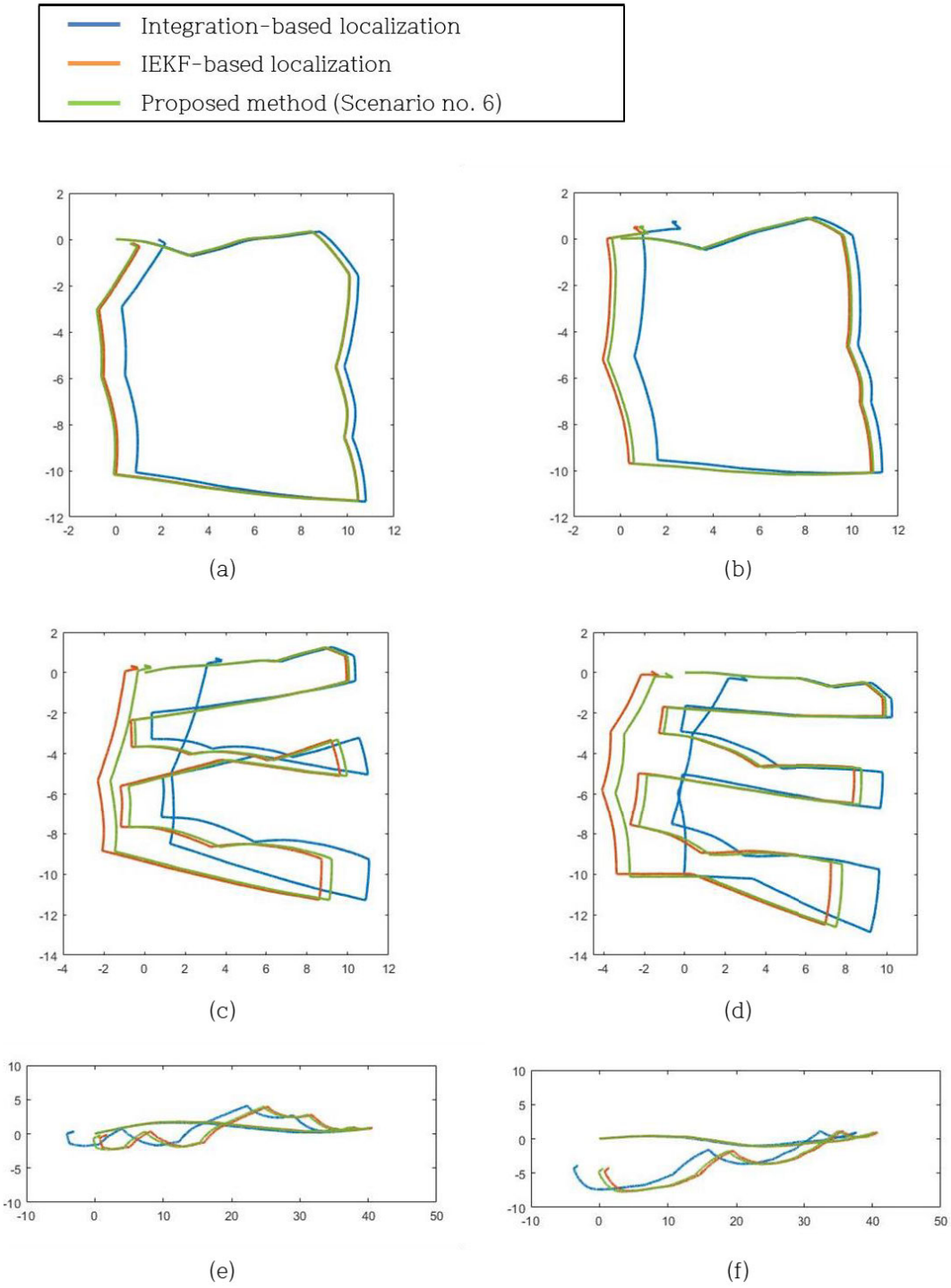

FIGURE 15. Trajectories of integration-based localization, IEKF-based localization, and proposed method for dataset no. 4-1, 4-3, 4-5, 4-7, 4-9, and 4-12.

substitute for real-world datasets in the training of the proposed network.

The proposed method estimates the slip ratio by analyzing sensor data patterns. While this method shows promising results compared to the integration-based localization and the IEKF-based localization, using multiple inertial sensors located in various positions could potentially improve its performance by providing more information. However, this approach can lead to longer computational times as input data are increased. In future work, we can investigate the

TABLE 6. Experimental results.

Dataset no.	Slope	Trajectory	Closed-loop error (m)							
			Integration-based localization	IEKF-based localization	Proposed method					
					S1	S2	S3	S4	S5	S6
4-1	Slope no. 5	Square	1.46	**0.45**	0.52	0.49	0.49	0.50	0.55	0.48
4-2			2.37	1.09	1.01	1.05	1.04	**0.98**	0.99	1.01
4-3			2.21	0.80	0.77	0.77	0.75	**0.72**	0.81	0.76
4-4			2.98	1.37	1.29	1.31	1.30	**1.24**	1.32	1.30
Average			2.25	0.92	0.90	0.90	0.89	**0.86**	0.92	0.89
4-5	Slope no. 5	Zigzag-pattern	3.78	1.18	1.13	1.13	1.13	1.13	**1.06**	1.13
4-6			2.05	**1.73**	1.89	1.89	1.91	2.11	1.96	1.84
4-7			2.80	1.40	1.17	1.19	1.19	1.40	1.30	**1.15**
4-8			3.58	1.15	**0.96**	0.97	0.97	1.01	**0.96**	0.97
Average			3.05	1.36	1.29	1.30	1.30	1.41	1.32	**1.27**
4-9	Slope no. 6	Straight-line	4.39	3.11	2.76	2.75	2.74	2.76	**2.65**	2.69
4-10			3.76	1.93	1.60	1.56	1.55	1.64	1.54	**1.51**
4-11			3.76	1.66	1.18	1.07	1.05	1.19	1.01	**0.99**
4-12			5.06	4.60	4.49	4.51	4.48	4.49	**4.41**	4.48
Average			4.24	2.83	2.51	2.47	2.45	2.52	**2.41**	2.42
Average for all datasets			3.18	1.71	1.56	1.56	**1.48**	1.60	1.55	1.53

TABLE 7. Computing time.

		Runtime (μs)
Integration-based localization		2.8
IEKF-based localization		38.9
Proposed method	Using GPU	622.5
	Using CPU	806.5

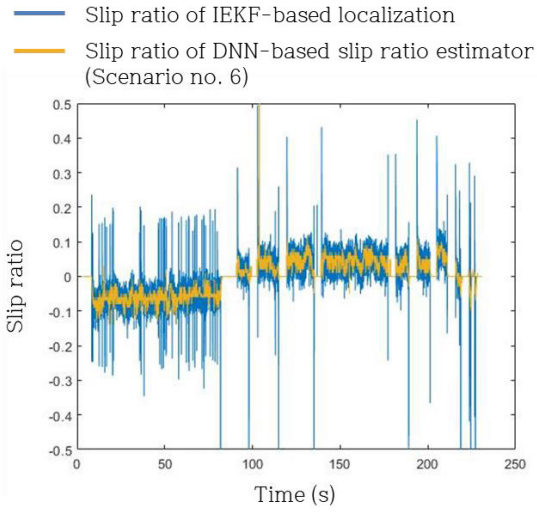

FIGURE 16. Example of slip ratio of IEKF-based localization and DNN-based slip ratio estimator for dataset no. 4-9.

trade-off between performance and computational time when using multiple sensors, which can provide insights into the benefits and limitations of this approach.

The proposed slip ratio estimator is trained using real-world datasets, which can be time-consuming and costly to generate for practical applications. To address this issue, one potential approach is to use simulated datasets as a substitute for real-world datasets. By substituting a portion of the real-world datasets with simulated datasets, significant effort and cost can be saved. In future work, we can investigate the use of simulated datasets to train the proposed slip ratio estimator. We can also investigate the trade-off between the ratio of real-world datasets and simulated datasets used in the training process. Additionally, it is important to evaluate the performance of the slip ratio estimator using simulated datasets and to compare it with the performance using real-world datasets.

VI. CONCLUSION

This paper proposed a DNN-based slip ratio estimator with IEKF for the localization of WMRs with lugged-wheels. Only an inertial sensor and an encoder were used. Instead of using the conventional slip model for lugged-wheels to estimate the slip ratio, the motion of lugged-wheels was analyzed using the Euler-Lagrange equation and concluded that data rates of the inertial sensor and encoder are insufficient to calculate the wheel slippage. The DNN-based slip ratio estimator, which is composed of a CNN, a FC layer, and a smoothing filter, was proposed to analyze the pattern of sensors to estimate the slip ratio. The estimated slip ratio was used as a pseudo measurement of the IEKF-based localization to estimate the robot pose. Dataset-based experiments were performed to evaluate the performance of the proposed localization, and results showed that the proposed method reduces the accumulated localization error of the integration-based localization by 53.5% and the IEKF-based localization by 13.5%. In future work, we plan to explore the potential benefits of using multiple inertial sensors positioned in various locations to improve the performance of the DNN-based slip ratio estimator, while considering the computational costs associated with processing the increased input data. Additionally, we will investigate the use of simulated

datasets as a substitute for real-world datasets in training the proposed network, which could reduce the time and cost requirements of generating real-world datasets for practical applications.

REFERENCES

[1] S. A. S. Mohamed, M. Haghbayan, T. Westerlund, J. Heikkonen, H. Tenhunen, and J. Plosila, "A survey on odometry for autonomous navigation systems," *IEEE Access*, vol. 7, pp. 97466–97486, 2019, doi: 10.1109/ACCESS.2019.2929133.

[2] Y. Su, T. Wang, S. Shao, C. Yao, and Z. Wang, "GR-LOAM: LiDAR-based sensor fusion SLAM for ground robots on complex terrain," *Robot. Auto. Syst.*, vol. 140, Jun. 2021, Art. no. 103759, doi: 10.1016/j.robot.2021.103759.

[3] D.-H. Yi, T.-J. Lee, and D.-I. Cho, "Afocal optical flow sensor for reducing vertical height sensitivity in indoor robot localization and navigation," *Sensors*, vol. 15, no. 5, pp. 11208–11221, May 2015, doi: 10.3390/s150511208.

[4] U. Onyekpe, V. Palade, A. Herath, S. Kanarachos, and M. E. Fitzpatrick, "WhONet: Wheel odometry neural network for vehicular localisation in GNSS-deprived environments," *Eng. Appl. Artif. Intell.*, vol. 105, Oct. 2021, Art. no. 104421, doi: 10.1016/j.engappai.2021.104421.

[5] D. Lhomme-Desages, C. Grand, F. B. Amar, and J.-C. Guinot, "Doppler-based ground speed sensor fusion and slip control for a wheeled rover," *IEEE/ASME Trans. Mechatronics*, vol. 14, no. 4, pp. 484–492, Aug. 2009, doi: 10.1109/TMECH.2009.2013713.

[6] J. Yi, H. Wang, J. Zhang, D. Song, S. Jayasuriya, and J. Liu, "Kinematic modeling and analysis of skid-steered mobile robots with applications to low-cost inertial-measurement-unit-based motion estimation," *IEEE Trans. Robot.*, vol. 25, no. 5, pp. 1087–1097, Oct. 2009, doi: 10.1109/TRO.2009.2026506.

[7] M. Maimone, Y. Cheng, and L. Matthies, "Two years of visual odometry on the Mars Exploration Rovers," *J. Field Robot.*, vol. 24, no. 3, pp. 169–186, Mar. 2007, doi: 10.1002/rob.20184.

[8] A. Angelova, L. Matthies, D. Helmick, and P. Perona, "Learning and prediction of slip from visual information," *J. Field Robot.*, vol. 24, no. 3, pp. 205–231, Mar. 2007, doi: 10.1002/rob.20179.

[9] C. Cunningham, M. Ono, I. Nesnas, J. Yen, and W. L. Whittaker, "Locally-adaptive slip prediction for planetary rovers using Gaussian processes," in *Proc. IEEE Int. Conf. Robot. Autom. (ICRA)*, Singapore, May 2017, pp. 5487–5494.

[10] R. Gonzalez, D. Apostolopoulos, and K. Iagnemma, "Slippage and immobilization detection for planetary exploration rovers via machine learning and proprioceptive sensing," *J. Field Robot.*, vol. 35, no. 2, pp. 231–247, Mar. 2018, doi: 10.1002/rob.21736.

[11] R. Gonzalez, S. Chandler, and D. Apostolopoulos, "Characterization of machine learning algorithms for slippage estimation in planetary exploration rovers," *J. Terramechanics*, vol. 82, pp. 23–34, Apr. 2019, doi: 10.1016/j.jterra.2018.12.001.

[12] C. Kilic, J. N. Gross, N. Ohi, R. Watson, J. Strader, T. Swiger, S. Harper, and Y. Gu, "Improved planetary rover inertial navigation and wheel odometry performance through periodic use of zero-type constraints," in *Proc. IEEE/RSJ Int. Conf. Intell. Robots Syst. (IROS)*, Macau, China, Nov. 2019, pp. 552–559.

[13] C. Kilic, N. Ohi, Y. Gu, and J. N. Gross, "Slip-based autonomous ZUPT through Gaussian process to improve planetary rover localization," *IEEE Robot. Autom. Lett.*, vol. 6, no. 3, pp. 4782–4789, Jul. 2021, doi: 10.1109/LRA.2021.3068893.

[14] U. Kono, H. Fujimoto, and Y. Hori, "Localization of wheeled mobile robots from slip ratio estimation with simple model," in *Proc. IEEE Int. Conf. Mechatronics (ICM)*, Kashiwa, Japan, Mar. 2021, pp. 1–6.

[15] P. Ravula, G. Acar, and B. Balachandran, "Discrete element method-based studies on dynamic interactions of a lugged wheel with granular media," *J. Terramechanics*, vol. 94, pp. 49–62, Apr. 2021, doi: 10.1016/j.jterra.2021.01.002.

[16] L. Ding, H. Gao, Z. Deng, K. Yoshida, and K. Nagatani, "Slip ratio for lugged wheel of planetary rover in deformable soil: Definition and estimation," in *Proc. IEEE/RSJ Int. Conf. Intell. Robots Syst.*, St. Louis, MO, USA, Oct. 2009, pp. 3343–3348.

[17] L. Ding, L. Huang, S. Li, H. Gao, H. Deng, Y. Li, and G. Liu, "Definition and application of variable resistance coefficient for wheeled mobile robots on deformable terrain," *IEEE Trans. Robot.*, vol. 36, no. 3, pp. 894–909, Jun. 2020, doi: 10.1109/TRO.2020.2981822.

[18] Z. Jia, W. Smith, and H. Peng, "Terramechanics-based wheel-terrain interaction model and its applications to off-road wheeled mobile robots," *Robotica*, vol. 30, no. 3, pp. 491–503, May 2012, doi: 10.1017/S0263574711000798.

[19] Y. Yuan, Q. Lan, L. Ding, H. Yang, H. Gao, Z. Wang, C. Yang, and Z. Deng, "Estimation of interaction forces with minimal parameters for rigid wheels on deformable terrain using modified Hooke's law," *Mechanism Mach. Theory*, vol. 169, Mar. 2022, Art. no. 104663, doi: 10.1016/j.mechmachtheory.2021.104663.

[20] Y. Du, J. Gao, L. Jiang, and Y. Zhang, "Numerical analysis of lug effects on tractive performance of off-road wheel by DEM," *J. Brazilian Soc. Mech. Sci. Eng.*, vol. 39, no. 6, pp. 1977–1987, Sep. 2016.

[21] J. Kim and J. Lee, "Traction-energy balancing adaptive control with slip optimization for wheeled robots on rough terrain," *Cognit. Syst. Res.*, vol. 49, pp. 142–156, Jun. 2018, doi: 10.1016/j.cogsys.2018.01.007.

[22] C. Cadena, L. Carlone, H. Carrillo, Y. Latif, D. Scaramuzza, J. Neira, I. Reid, and J. J. Leonard, "Past, present, and future of simultaneous localization and mapping: Toward the robust-perception age," *IEEE Trans. Robot.*, vol. 32, no. 6, pp. 1309–1332, Dec. 2016, doi: 10.1109/TRO.2016.2624754.

[23] Y. Pan, P. Xiao, Y. He, Z. Shao, and Z. Li, "MULLS: Versatile LiDAR SLAM via multi-metric linear least square," in *Proc. IEEE Int. Conf. Robot. Autom. (ICRA)*, Xi'an, China, May 2021, pp. 11633–11640.

[24] Z. Teed and J. Deng, "DROID-SLAM: Deep visual SLAM for monocular, stereo, and RGB-D Cameras," in *Proc. Adv. Neural Inf. Process. Syst. (NIPS)*, 2021, pp. 16558–16569.

[25] X. Lin, F. Wang, L. Guo, and W. Zhang, "An automatic key-frame selection method for monocular visual odometry of ground vehicle," *IEEE Access*, vol. 7, pp. 70742–70754, 2019, doi: 10.1109/ACCESS.2019.2916901.

[26] Y. Wu, J. Kuang, X. Niu, J. Behley, L. Klingbeil, and H. Kuhlmann, "Wheel-SLAM: Simultaneous localization and terrain mapping using one wheel-mounted IMU," *IEEE Robot. Autom. Lett.*, vol. 8, no. 1, pp. 280–287, Jan. 2023, doi: 10.1109/LRA.2022.3226071.

[27] T.-J. Lee, C.-H. Kim, and D.-I. Dan Cho, "A monocular vision sensor-based efficient SLAM method for indoor service robots," *IEEE Trans. Ind. Electron.*, vol. 66, no. 1, pp. 318–328, Jan. 2019, doi: 10.1109/TIE.2018.2826471.

[28] G. Yang, L. Zhao, J. Mao, and X. Liu, "Optimization-based, simplified stereo visual-inertial odometry with high-accuracy initialization," *IEEE Access*, vol. 7, pp. 39054–39068, 2019, doi: 10.1109/ACCESS.2019.2902295.

[29] C. Campos, R. Elvira, J. J. G. Rodríguez, J. M. M. Montiel, and J. D. Tardós, "ORB-SLAM3: An accurate open-source library for visual, visual-inertial, and multimap SLAM," *IEEE Trans. Robot.*, vol. 37, no. 6, pp. 1874–1890, Dec. 2021, doi: 10.1109/TRO.2021.3075644.

[30] Y. Zhang, "LILO: A novel LiDAR–IMU SLAM system with loop optimization," *IEEE Trans. Aerosp. Electron. Syst.*, vol. 58, no. 4, pp. 2649–2659, Aug. 2022, doi: 10.1109/TAES.2021.3135234.

[31] J. Zhu, Y. Tang, X. Shao, and Y. Xie, "Multisensor fusion using fuzzy inference system for a visual-IMU-wheel odometry," *IEEE Trans. Instrum. Meas.*, vol. 70, pp. 1–16, 2021, doi: 10.1109/TIM.2021.3051999.

[32] W. Qi, S. E. Ovur, Z. Li, A. Marzullo, and R. Song, "Multi-sensor guided hand gesture recognition for a teleoperated robot using a recurrent neural network," *IEEE Robot. Autom. Lett.*, vol. 6, no. 3, pp. 6039–6045, Jul. 2021, doi: 10.1109/LRA.2021.3089999.

[33] W. Qi and A. Aliverti, "A multimodal wearable system for continuous and real-time breathing pattern monitoring during daily activity," *IEEE J. Biomed. Health Informat.*, vol. 24, no. 8, pp. 2199–2207, Aug. 2020, doi: 10.1109/JBHI.2019.2963048.

[34] Y. Shi, J. Chang, Y. Wang, X. Zhao, Q. Zhang, and L. Yang, "Gas leakage detection and pressure difference identification by asymmetric differential pressure method," *Chin. J. Mech. Eng.*, vol. 35, no. 1, p. 44, Apr. 2022.

[35] Y. Shi, M. Cai, W. Xu, and Y. Wang, "Methods to evaluate and measure power of pneumatic system and their applications," *Chin. J. Mech. Eng.*, vol. 32, no. 1, pp. 1–11, May 2019.

[36] G. Yang, J. Yao, and Z. Dong, "Neuroadaptive learning algorithm for constrained nonlinear systems with disturbance rejection," *Int. J. Robust Nonlinear Control*, vol. 32, no. 10, pp. 6127–6147, Jul. 2022, doi: 10.1002/rnc.6143.

[37] M. Brossard and S. Bonnabel, "Learning wheel odometry and IMU errors for localization," in *Proc. Int. Conf. Robot. Autom. (ICRA)*, Montreal, QC, Canada, May 2019, pp. 291–297.

[38] M. Brossard, A. Barrau, and S. Bonnabel, "AI-IMU dead-reckoning," *IEEE Trans. Intell. Vehicles*, vol. 5, no. 4, pp. 585–595, Dec. 2020, doi: 10.1109/TIV.2020.2980758.

[39] S. Herath, H. Yan, and Y. Furukawa, "RoNIN: Robust neural inertial navigation in the wild: Benchmark, evaluations, & new methods," in *Proc. IEEE Int. Conf. Robot. Autom. (ICRA)*, Paris, France, May 2020, pp. 3146–3152.

[40] J. Jiao, J. Jiao, Y. Mo, W. Liu, and Z. Deng, "MagicVO: An end-to-end hybrid CNN and bi-LSTM method for monocular visual odometry," *IEEE Access*, vol. 7, pp. 94118–94127, 2019, doi: 10.1109/ACCESS.2019.2926350.

[41] M. Brossard, S. Bonnabel, and A. Barrau, "Denoising IMU gyroscopes with deep learning for open-loop attitude estimation," *IEEE Robot. Autom. Lett.*, vol. 5, no. 3, pp. 4796–4803, Jul. 2020, doi: 10.1109/LRA.2020.3003256.

[42] D. Morin, "The Lagrangian method," in *Introduction to Classical Mechanics: With Problems and Solutions*. Cambridge, U.K.: Cambridge Univ. Press, 2008, ch. 6. [Online]. Available: https://scholar.harvard.edu/

[43] A. Barrau and S. Bonnabel, "The invariant extended Kalman filter as a stable observer," *IEEE Trans. Autom. Control*, vol. 62, no. 4, pp. 1797–1812, Apr. 2017, doi: 10.1109/TAC.2016.2594085.

[44] A. Barrau and S. Bonnabel, "Invariant Kalman filtering," *Annu. Rev. Control, Robot., Auto. Syst.*, vol. 1, no. 1, pp. 237–257, May 2018, doi: 10.1146/annurev-control-060117-105010.

[45] *MPU-6000 and MPU-6050 Product Specification Revision 3.3*, document PS-MPU-6000A-00, InvenSense, CA, USA, May 2012. [Online]. Available: https://pdf1.alldatasheet.com/datasheet-pdf/view/517744/ETC1/MPU-6050.html

CHUL-HONG KIM received the Bachelor of Science degree from Australian National University, Australia, in 2014. He is currently pursuing the Ph.D. degree with the Department of Electrical and Computer Engineering, Seoul National University, South Korea.

His research interests include robot vision, robot localization, SLAM, and deep learning.

DONG-IL (DAN) CHO received the Bachelor of Science degree from Carnegie Mellon University, USA, in 1980, and the Master of Science and Ph.D. degrees from the Massachusetts Institute of Technology, USA, in 1984 and 1988, respectively.

From 1987 to 1993, he was an Assistant Professor with the Department of Mechanical and Aerospace Engineering, Princeton University, USA. Since 1993, he has been an Assistant Professor, an Associate Professor, and a Full Professor with the Department of Electrical and Computer Engineering, Seoul National University, South Korea. He has published over 150 journal articles and 150 patents. His research interests include the nonlinear and intelligent control of robotic and mechatronic systems, MEMS-fabrication, and sensor technologies. He has served on the editorial board of many international journals, including the Co-Editor-in-Chief for *Mechatronics* (IFAC) and a Senior Editor for IEEE JOURNAL OF MICROELECTROMECHANICAL SYSTEMS. He has served as the President for ICROS and a BOG Member for IEEE CSS and EDS. He is currently the President-Elect of IFAC and will be the President, from 2023 to 2026. He was elected as an Ordinary Member (2010–2012) and a Senior Member (2013–2017) and (since 2018) of the National Academy of Engineering of Korea.